JOURNAL OF THE ROYAL SOCIETY Interface

rsif.royalsocietypublishing.org

Research

Cite this article: Leemreize H, Almer JD, Stock SR, Birkedal H. 2013 Three-dimensional distribution of polymorphs and magnesium in a calcified underwater attachment system by diffraction tomography. J R Soc Interface 10: 20130319.
http://dx.doi.org/10.1098/rsif.2013.0319

Received: 8 April 2013
Accepted: 4 June 2013

Subject Areas:
biomaterials, biogeochemistry

Keywords:
diffraction tomography, hierarchical materials, biomineralization, calcium carbonate, magnesium substitution

Authors for correspondence:
Stuart R. Stock
e-mail: s-stock@northwestern.edu
Henrik Birkedal
e-mail: hbirkedal@chem.au.dk

Royal Society Publishing
Informing the science of the future

Three-dimensional distribution of polymorphs and magnesium in a calcified underwater attachment system by diffraction tomography

Hanna Leemreize[1], Jonathan D. Almer[2], Stuart R. Stock[3] and Henrik Birkedal[1]

[1]iNANO and Department of Chemistry, Aarhus University, 14 Gustav Wieds Vej, Aarhus 8000, Denmark
[2]X-ray Science Division, Argonne National Laboratory, 9700 S. Cass Avenue, Argonne, IL 60439, USA
[3]Department of Molecular Pharmacology and Biological Chemistry, Feinberg School of Medicine, Northwestern University, 303 East Chicago Avenue, Chicago, IL 60611-3008, USA

Biological materials display complicated three-dimensional hierarchical structures. Determining these structures is essential in understanding the link between material design and properties. Herein, we show how diffraction tomography can be used to determine the relative placement of the calcium carbonate polymorphs calcite and aragonite in the highly mineralized holdfast system of the bivalve *Anomia simplex*. In addition to high fidelity and non-destructive mapping of polymorphs, we use detailed analysis of X-ray diffraction peak positions in reconstructed powder diffraction data to determine the local degree of Mg substitution in the calcite phase. These data show how diffraction tomography can provide detailed multi-length scale information on complex materials in general and of biomineralized tissues in particular.

1. Introduction

The performance of biological materials depends crucially on their hierarchical structure [1–3]. Understanding these structures is thus paramount to understanding how and why the materials work. Techniques used to probe these structures should preferably be able to probe the interior of the sample on several length scales without requiring destructive sample preparation. One of the few techniques fulfilling this requirement is micro-computed tomography (μCT). In standard μCT, three-dimensional images of the sample linear attenuation coefficients are reconstructed based on a series of projection images [4]. Higher contrast between materials with similar absorption power can be obtained by employing phase contrast, which is sensitive to the X-ray refractive index rather than only absorption [5,6]. Ptychography also provides high contrast refractive index maps [7]. However, none of these imaging modalities directly distinguish different crystalline materials with similar effective absorptivity and refractive index within a complex mixture. In $CaCO_3$ biominerals, for example, a mixture of the polymorphs aragonite and calcite are often observed in conjunction with an organic matrix. Until very recently, it has only been possible to map polymorph distributions by methods requiring destructive sample preparation such as position-resolved X-ray diffraction [8–10], confocal Raman scattering [10] or similar techniques.

Here, we employ an alternative tomographic technique to map polymorphs in a calcified biomineral structure. This is done using diffraction tomography that is based on collecting position-resolved diffraction data at many angular orientations of the specimen. This technique allows for reconstruction of the three-dimensional distribution of crystallographic phases [11–15]. This method is complementary to grain-resolved X-ray techniques, i.e. 'high-energy diffraction microscopy' [16] or '3DXRD' [17,18], which require little or no diffraction spot overlap and thus are mainly applicable to larger (>μm) grained materials than

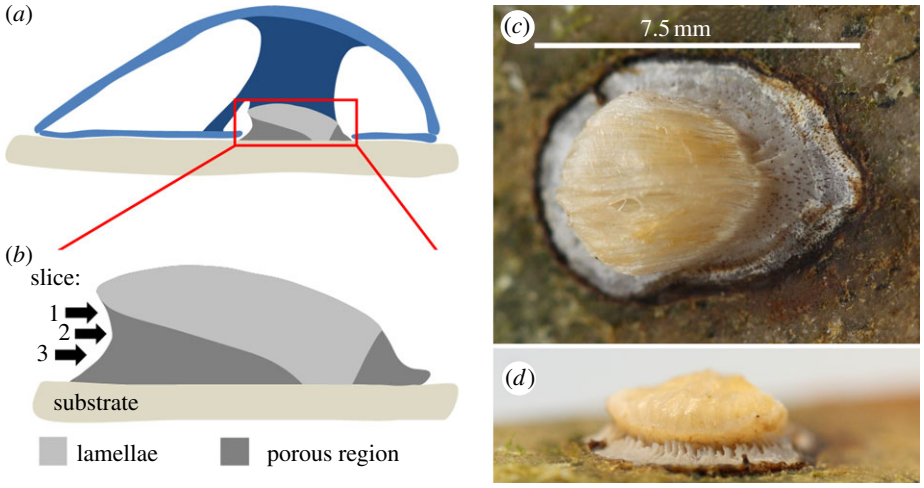

Figure 1. The *Anomia* byssus. (*a*,*b*) Sketches of a cross-section of the animal along its long axis. Schematic (*a*) shows the placement of the byssus in the animal. Light blue indicates the shell while the dark blue displays the byssus retractor muscle and the adductor muscle. Schematic (*b*) highlights the division of the byssus structure into a lamellar and a porous part and also indicates the positions of the three slices investigated by diffraction tomography in the present work. (*c*,*d*) Photographs of a byssus attached to a stone. Image (*c*) is recorded from above the substrate and shows the lamellar interface to the musculature. The pores extending from the top of the porous region to the substrate are visible as brown colorations on the surface of the porous part. (*d*) Byssus from behind towards the tip of the byssal notch. Channels approximately parallel to the substrate are seen extending into the byssus.

those studied here. We show how diffraction tomography can be applied to highly complex $CaCO_3$ biomineral structures yielding not only maps of polymorphs but also of the local degree of Mg substitution, which can be determined from the local lattice constants because Mg substitution leads to known changes in the calcite lattice constants [19].

An important area where biological materials prove their mettle is in underwater adhesion with the mussel byssus [20,21], oysters [22] and barnacles [23] as prime examples. Contrary to the protein-based byssus of the Mytilidae [20,21], *Anomia simplex* uses a highly calcified (more than 90 wt%) byssus that extends through a notch in the right valve [24–30]. The byssus has a highly complex hierarchical structure [28,29,31], where both aragonite and calcite are present [24,26,28,29,31]. It consists of a lamellar part that forms the interface with the musculature of the animal and a porous part closer to the substrate as seen in figure 1. There is an array of large channels that extend roughly parallel to the substrate–byssus interface and branch out into many smaller pores that extend vertically down to the substrate, figure 1*d*. The large channels reach the substrate close to where the lamellar part reaches the substrate, figure 1*b*. Additional small perpendicular pores are also seen around edges of the byssus extending from the outer surface all the way down to the substrate [24,29], as can be seen in figure 1*c*.

The lamellar part consists of sheets of organic material decorated with a herringbone arrangement of crystals [29]. The organic sheets penetrate into the musculature of the animal and maximize the contact area. The organic sheets also extend all the way through the byssus to the substrate, which highlights the structural importance of these sheets. Their role in the formation process of the byssus was studied by Yamaguchi in *Anomia chinensis* [24]. When the juvenile animal settles, the foot initially deposits a small lamellar organic plate that mineralizes during the juvenile stage of the animal (figure 2*a*). When the animal grows, the byssus also enlarges by addition of a larger lamellar pad above the previous byssus height within the animal. Near the substrate, this enlarged pad is supported by addition of the

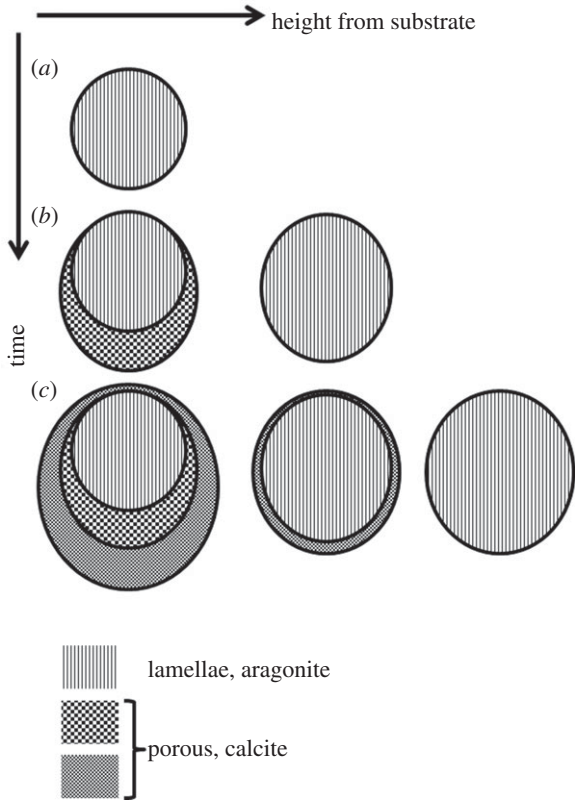

Figure 2. Sketch of the growth of *Anomia* byssi derived from the work of Yamaguchi [24]. Sketches of cross sections parallel to the substrate are shown at different stages of animal growth along the vertical axis and at different heights from the substrate along the horizontal axis. Vertically striated sections indicate aragonitic lamellae while the checkerboard patterns represent the calcitic porous part of the byssus.

porous calcite (figure 2*b*). When the animal grows even more, an additional, even larger lamellar pad is added on top with corresponding calcitic support structures beneath (figure 2*c*). This leads to the complex morphology seen in figure 1.

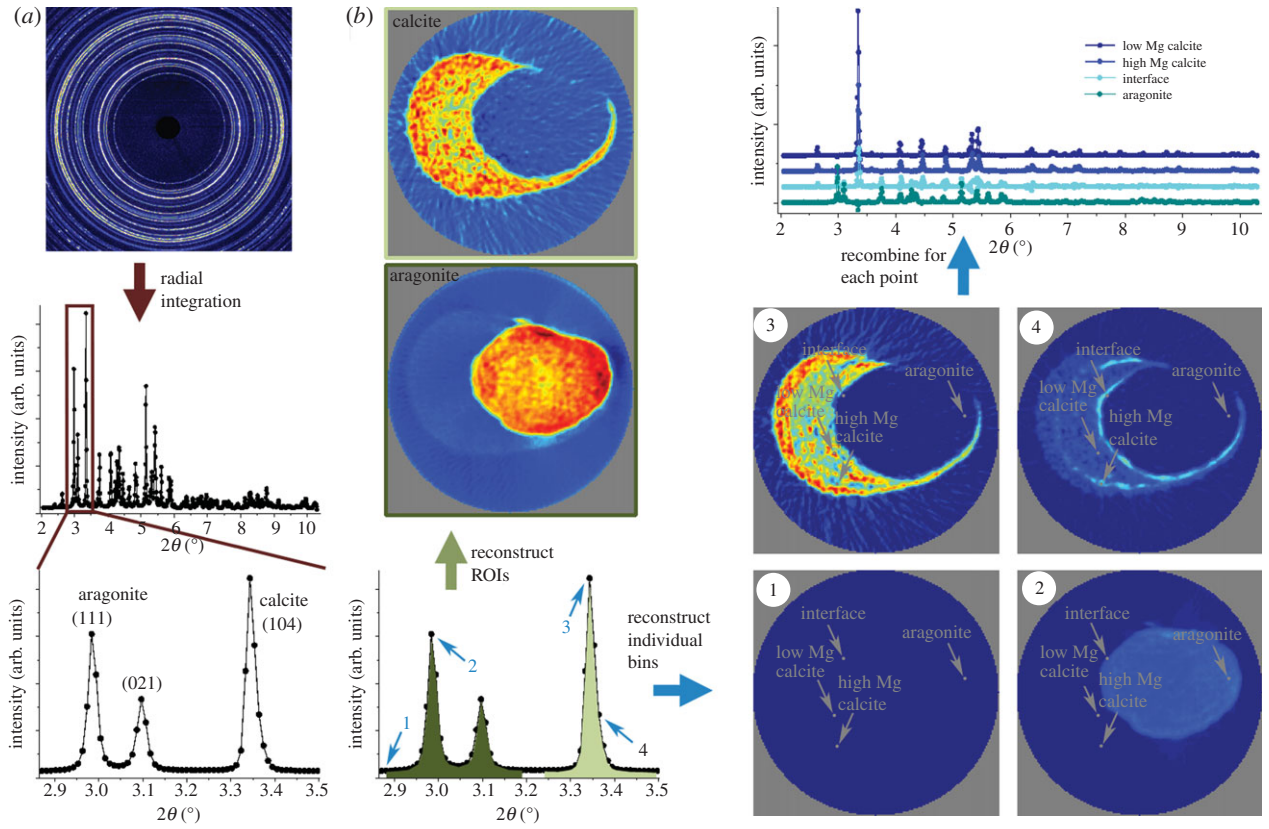

Figure 3. Schematic of the data treatment procedure used for the diffraction data; illustrated by using data from slice 2. (*a*) The raw data that have been radially integrated to give powder patterns. A zoom of the part of the powder pattern that is in focus in the rest of the analysis is shown in the lower image—this part of the powder pattern is shown again to the right in (*b*) highlighting the regions of interests (ROIs) used in the analysis. As a measure of the amount of the two polymorphs of $CaCO_3$ in the sample, the summed intensity across the aragonite (111) and (021) peaks (dark green ROI) and the calcite (104) peak (light green ROI) are used. These sums are reconstructed to give the polymorph maps shown at the top left of (*b*) and in figure 4 for all slices (the diameter of the field of view is 8 mm). Individual 2θ bins can also be used as ROIs and be reconstructed. A few examples of this (from the bins highlighted with blue arrows) are shown in the bottom right of (*b*). When all 2θ bins have been reconstructed, the intensity in each from one single voxel (x, y, z) can be recombined to give the entire diffractogram from this voxel. Examples from the voxels highlighted with the grey arrows are shown in the top of the right column in (*b*) and in figure 5.

2 Experimental

2.1. Animals

Live specimens of *Anomia simplex* were obtained from Woods Hole Marine Biological Laboratory (Woods Hole, MA, USA); they were sacrificed upon arrival by placing them in a −18°C freezer. The sample was extracted mechanically from an animal attached to a stone and briefly washed in 70 per cent ethanol. It measured about $9 \times 6\ mm^2$ at the substrate interface and $7–8 \times 4\ mm^2$ higher up, where diffraction tomography measurements were performed (see below).

2.2. Synchrotron X-ray absorption and diffraction tomography

Synchrotron radiation absorption and diffraction tomography data were measured at beamline 1-ID at the Advanced Photon Source (APS, Argonne National Laboratory, Argonne, IL, USA) using 70 keV X-rays and a $50 \times 50\ \mu m^2$ beam. The sample was mounted so that the rotation axis of the goniometer was perpendicular to the substrate plane; hence, tomography slices were parallel to the substrate plane. For each angular orientation, diffraction data were collected at 160 positions with 50 µm intervals yielding an isotropic voxel size of $50 \times 50 \times 50\ \mu m^3$ in the reconstructions. For each slice, 161 projections covering 0–360° in 2.25° intervals were measured. Diffraction patterns were detected using a General Electric Angio amorphous Si two-dimensional detector at a nominal sample-detector distance of 1118 mm, and calibrated to account for beam centre and tilting relative to the Debye ring using a CeO_2 standard and established procedures [11]. Sample absorption was measured by comparing the signal from a PIN diode mounted in the beamstop to that of an ion chamber before the specimen.

Two-dimensional diffraction patterns were obtained in a given spatial (y', z') and angular position (ϕ) of the sample as exemplified by the data shown in figure 3*a*. Small but systematic intensity variations around the Debye ring revealed a weak crystallographic texture. In the calibrated two-dimensional data, the intensity was a function of diffraction angle, position, sample angular position and azimuthal angle (2θ, y', z', ϕ, χ). The two-dimensional diffractograms were integrated over the full azimuthal angle (χ) to yield powder patterns depending on the position and sample angular position (2θ, y', z', ϕ) (figure 3*a*). By averaging over many orientations, this angular integration minimizes any effects of texture on the results obtained. Slices were reconstructed in two ways, both using a filtered backprojection. Software for azimuthal integration, tomographic reconstructions, data fitting and plotting was developed in-house in MATLAB (MathWorks, Natick, MA)

In the first reconstruction approach, regions of interest (ROIs) in 2θ were defined. The intensities in the ROIs were

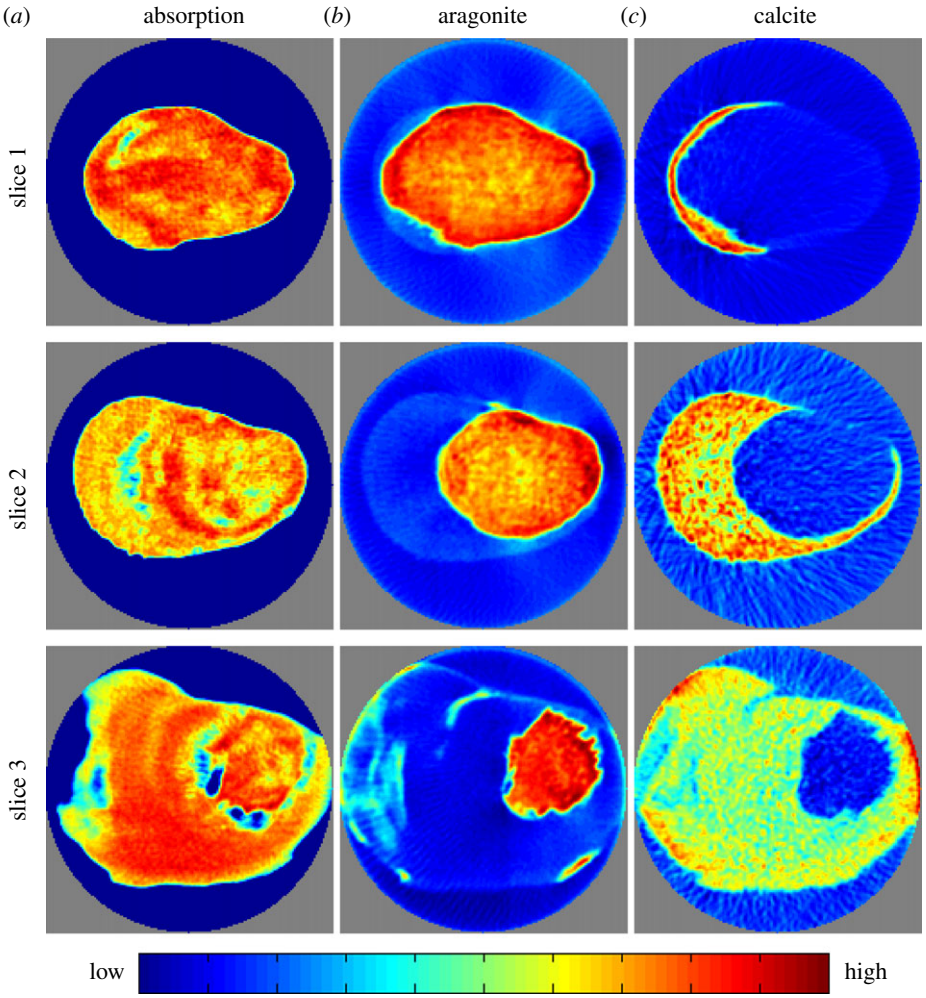

Figure 4. Reconstructed slices based on X-ray absorption (*a*) and X-ray diffraction tomography (*b*,*c*). The diameter of the field of view is 8 mm. The latter show the distribution of aragonite and calcite, respectively. The slice numbers refer to the sketch in figure 1*b*. Grey voxels are the voxels outside of the field of view of the experiment.

integrated and reconstructed to yield maps of ROIs in real space ($I(\mathrm{ROI}(2\theta), x, y, z)$). Selecting two ROIs corresponding to the calcite (104) (light green in figure 3*b*) and the aragonite (111) and (021) (dark green in figure 3*b*) diffraction peaks results in maps of polymorph distributions as shown in figure 3*b* and the last two columns of figure 4. Note that the intensities in these maps are not on an absolute scale and hence not directly comparable for different ROIs. These reconstructions assume that the crystallites are randomly oriented within the material. If this is not fulfilled not all crystals will be equally 'visible' depending on their orientation with respect to the X-ray beam. Hence, a textured phase will give rise to variations in the apparent amount of this polymorph in the maps. This effect is especially obvious for the calcite phase, which displays a significantly larger degree of texture than the aragonite phase.

In the second reconstruction strategy, fully reconstructed diffraction patterns were obtained by reconstructing each bin in 2θ space to yield fully reconstructed powder diffractograms in real space ($I(2\theta, x, y, z)$). The procedure for this is sketched in figure 3*b* using blue arrows while selected diffractograms are shown in figure 3*b* and figure 5*b*,*c*.

It is worth commenting on the angular resolution of the diffractograms. The detector pixel size, 200 µm, leads to an angular resolution of 0.01° 2θ at the position of the calcite (104) peak, corresponding to a $\Delta d/d$ of 0.003. However, since the sample is relatively large, motional averaging induced by rotation of the specimen during the measurements leads to additional broadening. Again referring to calcite (104), the maximal effect of this motional averaging comes from a contributing crystallite located at the sample surface. The present field of view of 8 mm then leads to a maximal motional averaging of 2.33 pixels. On average, the effect will be smaller. For the two main aragonite peaks, we obtain an average FWHM of ~2.8 pixels. We note that the maximal motional averaging is smaller than the shifts used to determine the Mg substitution.

The local Mg content was obtained by analysis of the calcite (104) peak position from the reconstructed powder diffractograms. Mg substitution leads to a known change in the calcite lattice constants whereas Mg does not substitute into the aragonite lattice [19]. A 2θ-range 2.87–3.50° encompassing the calcite (104) and the aragonite (111) and (021) diffraction peaks was selected for analysis. The angular positions (*d*-spacings) of the aragonite diffraction peaks did not change with position within the sample. The calcite (104) peak, however, is shifted significantly as expected for the varying degree of Mg substitution, as seen from the patterns shown in figure 5*c*. These shifts are also observed when comparing different (ray integrated) diffractograms, and in powder diffractograms on pulverized byssi. In the latter case, a very clear shoulder toward high angles is observed [29,31]. Diffractograms

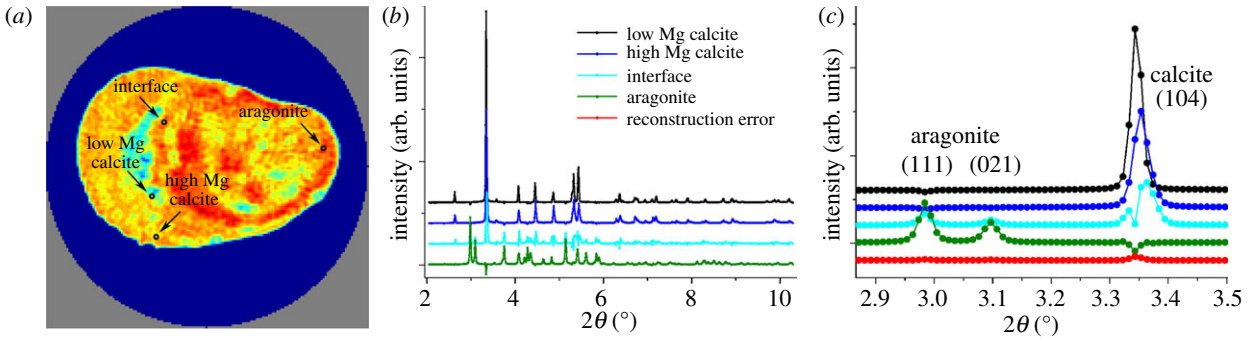

Figure 5. Reconstructed diffractograms from slice 2. Four one-dimensional diffractograms obtained in the voxels indicated in (*a*) are shown in (*b*,*c*) that show the full and a selected diffraction angle range, respectively. The image in (*a*) is the absorption-contrast reconstructed slice from figure 3.

reconstructed outside the sample should be featureless. However, due to reconstruction errors, they display non-zero values at the positions of the dominant diffraction peaks within the sample. Therefore, we used the average reconstructed diffractogram outside the sample (but within the field of view) as a measure of the precision of the data as a function of 2θ, i.e. their standard uncertainty (s.u.).

The major source of systematic error in the diffraction peak positions is imprecision in the determination of the average overall sample to detector distance. We compensated for this error by using the aragonite phase as an internal standard and assuming that its lattice parameters are the same as those found for biogenic aragonite from similar organisms. We calculated the expected peak positions of the aragonite (111) and (021) peaks from the lattice constants from biogenic aragonite from Bivalvia living in sea water [32]. Then an effective zero shift was determined by requiring that the observed peak positions in an average diffractogram of the entire sample matched the biogenic ones. This shift was then applied to the calcite peak positions; the zero point effectively corrects a sample to detector distance error because the high energy makes the diffraction peaks occur in a narrow range of small angles. The local Mg content was determined by weighted least squares against the distance-corrected data using the reconstruction errors as weights. As each voxel contains calcite with a range of Mg substitution, it was not possible to model the calcite (104) diffraction peak using a single peak and fitting its position. The distribution of Mg substitution was instead modelled using four Gaussian calcite (104) peaks with peak positions consistent with Mg contents of 0, 4, 8 and 12 mol% Mg, respectively. Their widths were constrained to be equal whereas their intensities were fitted independently. The effective Mg content was calculated from the relative intensities of the different Mg–calcite peaks. We have previously used this method on powdered byssus samples [31].

The s.u. of the Mg content was determined by error propagation of the s.u.'s of the intensities from the weighted least-squares fit. Besides the Mg–calcite (104) peaks, two Gaussian peaks fitting the aragonite (111) and (021) peaks and a background value were fitted.

3. Results

We performed diffraction tomography using high-energy X-rays (70 keV). These suffer little attenuation when traversing the specimen (up to 9 mm thick) and produce strong diffraction patterns; the measured transmission was in the range 28–45%. We collected and reconstructed data from three slices parallel to the byssus–substrate interface with isotropic voxel sizes of 50 µm as illustrated in figure 1 (see §2 for details). Both absorption and diffraction data were collected simultaneously. The first column of figure 4 displays the map of X-ray absorption in the three slices. Areas of low X-ray absorption correspond to pores and channels in the byssus. Besides these macroscopic features, the X-ray absorption images were almost featureless, at least at the current spatial resolution, and did not yield information on polymorph distribution as these have very similar linear attenuation coefficients.

The diffraction data on the other hand gave a wealth of information. The calcite and aragonite distributions were obtained by reconstructions using the azimuthally integrated intensities of selected isolated diffraction peaks. The resulting crystallographic phase maps are also shown in figure 4. It is immediately clear that the two polymorphs occupy distinct and disjoint parts of the byssus with aragonite being exclusively present in the lamellar part of the byssus while calcite makes up the porous part.

Full powder diffraction patterns could also be reconstructed for each voxel as shown in figure 5. Inspection of these reconstructed patterns (figure 5*b*,*c*) shows shifts in the calcite diffraction peaks at different positions within the byssus while the aragonite peaks stay at the same diffraction angle. It is well known that bio-calcites often are Mg substituted, and this is indeed also the case for the *Anomia simplex* byssus [29]. Mg substitution leads to a reduction in the calcite lattice constants thus resulting in a shift in diffraction peaks to higher 2θ angles. The peak shifts were used to create maps of the local degree of Mg substitution by fitting the calcite (104) peak (see §2 for details). The resulting maps and their associated errors are shown in figure 6 for the three slices through the byssus. The degree of Mg substitution thus determined was in most cases highly statistically significant, showing that the present diffraction tomography method is capable of yielding detailed insights into substitution chemistry in bio-calcite.

The Mg content in the byssus was found to vary from 0 to 10 per cent in the investigated sections. The experimental maps show that Mg substitution occurs in spatially distinct regions as was also previously observed by energy-dispersive X-ray spectroscopy (EDX) on polished sections [29]. Bands of higher Mg content are, for example, observed in calcite near the aragonite. Histograms of the Mg content for the three sections (figure 6*b*) show that the Mg contents

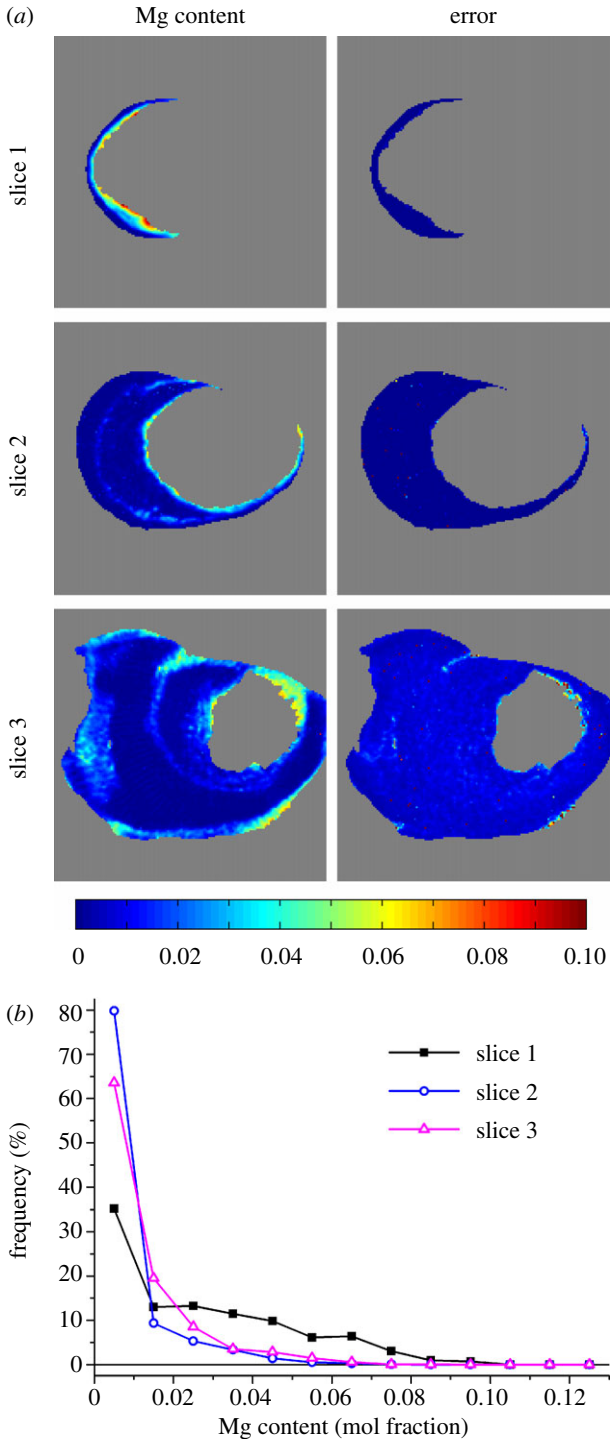

Figure 6 Magnesium substitution maps (*a*) determined by analysis of peak shifts of the calcite (104) peak in reconstructed diffractograms with the left column representing Mg content in mol% while the right column displays the associated standard uncertainty. Grey voxels are voxels where no calcite is present. (*b*) Mg content frequency distributions based on the maps in (*a*). The thin horizontal line represents zero frequency.

of slices 2 and 3 are very similar, whereas slice 1 has significantly larger amounts of calcite containing a higher degree of Mg substitution. This is partially because of the small amount of calcite in slice 1 with only the high Mg-containing band at the interface to the aragonitic region, but also because the degree of Mg substitution in this slice is generally larger as compared with the others. The maximum degree of Mg substitution in slices 2 and 3 is approximately 6 per cent whereas it is 10 per cent in slice 1 corresponding to $Ca_{0.9}Mg_{0.1}CO_3$.

4. Discussion

The tomographic reconstruction of full diffractograms allows for extraction of the detailed information about the crystalline phases contained in these diffractograms. In the present case, this analysis determined the distribution of Mg substitution in biogenic calcite, but the methodology can easily be extended to other types of analyses.

We stress that the samples were not sectioned or cut in any way prior to measurements. Note also that it would not have been possible to determine the degree of Mg substitution without destructive preparation by other techniques such as EDX. Non-destructive synchrotron X-ray fluorescence tomography [33,34] would likewise have been impossible because the large size and high degree of mineralization of the sample would have led to complete absorption of emitted Mg X-ray photons, the Mg *K*α attenuation length being only 1.5 µm for calcite. This effect would further be exacerbated by the high-air absorption of Mg X-rays that would require vacuum or helium environments around the sample [35].

The Mg distributions observed in the byssus may be caused by two distinct biological phenomena: an adaption of local structure to meet a mechanical demand or as a by product of byssus growth. Mg-substituted calcite is stiffer than Mg-free calcite [36], and such substitution may tune local mechanical properties to mechanical requirements. This has been suggested to be the case for sea urchin teeth that display very large, up to 40 per cent, degrees of Mg substitution.

Alternatively, Mg substitution can occur during calcite formation due to the presence of Mg in the precipitating medium. Sea water contains significant amounts of Mg. 'Accidental' substitution owing to direct precipitation of infiltrating sea water has been suggested to be the origin of Mg substitution in oyster cement that forms by crystallization of sea water in an organic matrix and displays degrees of Mg substitution of 7–10.4% [22] comparable to the ones observed in the high Mg regions of the *Anomia* byssus in the present work. The average Mg content determined in the present work is 1.13 per cent in the three slices but is much higher than the average near the interface with aragonite.

Recalling the byssus growth dynamics sketched in figure 2, it is clear from the data on slice 1 that when a new calcite portion is formed at a given height, Mg-rich calcite is deposited close to the lamellar/porous interface. We note that the microstructure in this region is different from that further away from the interface in that the calcite crystal aggregates are smaller [29]. The higher Mg content close to the interface may result from rejection of Mg during aragonite precipitation and its incorporation into the calcite growing nearby or from control of the precipitating liquid. In either case, the Mg content falls off with distance from the interface. When a new growth process starts, a new line of high-Mg-content calcite would be put down as observed in slices 2 and 3. In this case, the Mg content would reflect the underlying animal growth dynamics. Under the reasonable assumption that animal growth is seasonal, the varying Mg content may additionally be a consequence of variations in average local water temperature. The Mg content in organic-matrix free precipitation of calcite also depends

on the precipitation temperature. At low temperatures, calcite incorporates less Mg than at higher temperatures [37].

5. Conclusion

To summarize, we have used high-energy X-ray diffraction tomography to map the distribution of $CaCO_3$ polymorphs in the heavily calcified byssus of *Anomia simplex*. Because diffraction tomography allows for the reconstruction of full diffraction patterns, it was possible to determine the local degree of Mg substitution thus significantly enhancing the diffraction tomography methodology. All of this was achieved without cutting in the sample or destroying it in any way. Because of the very high X-ray energy used, the sample suffers minimal radiation damage and can hence be analysed using different techniques afterwards.

While the mechanism for the observed significant and systematic variations in the degree of Mg substitution remains unresolved, it clearly results in systematic variations in chemical composition and microstructure. The impact of these factors on byssus mechanical performance is under investigation.

Acknowledgements. We thank the Human Frontiers Science Program (HFSP), the Danish Council for Independent Research—Natural Sciences and the Graduate School of Science and Technology (GSST) of Aarhus University for funding.

Funding statement. S.R.S. acknowledges support from NICDR grant no. DE001374 (to Arthur Veis). Use of the Advanced Photon Source was supported by the US Department of Energy, Office of Science, Office of Basic Energy Sciences, under Contract no. DE-AC02-06CH11357.

References

1. Meyers MA, Chen P-Y, Lin AY-M, Seki Y. 2008 Biological materials: structure and mechanical properties. *Progr. Mater. Sci.* **53**, 1–206. (doi:10.1016/j.pmatsci.2007.05.002)
2. Miserez A, Weaver JC, Pedersen PB, Schneeberk T, Hanlon RT, Kisailus D, Birkedal H. 2009 Microstructural and biochemical characterization of the nanoporous sucker rings from *Dosidicus gigas* **21**, 401–406. (doi:10.1002/adma.200801197)
3. Fratzl P, Weinkamer R. 2007 Nature's hierarchical materials. *Progr. Mater. Sci.* **52**, 1263–1334. (doi:10.1016/j.pmatsci.2007.06.001)
4. Stock SR. 2008 *MicroComputed tomography: methodology and applications*. Boca Raton, FL: CRC Press.
5. Langer M, Pacureanu A, Suhonen H, Quentin G, Cloetens P, Peyrin F. 2012 X-ray phase nanotomography resolves the 3D human bone ultrastructure. *PLoS ONE* **7**, e35691. (doi:10.1371/journal.pone.0035691)
6. Cloetens P, Ludwig W, Baruchel J, Van Dyck D, Van Landuyt J, Guigay JP, Schlenker M. 1999 Holotomography: quantitative phase tomography with micrometer resolution using hard synchrotron radiation X rays. *Appl. Phys. Lett.* **75**, 2912–2914. (doi:10.1063/1.125225)
7. Dierolf M, Menzel A, Thibault P, Schneider P, Kewish CM, Wepf R, Bunk O, Pfeiffer F. 2010 Ptychographic X-ray computed tomography at the nanoscale. *Nature* **467**, 436–439. (doi:10.1038/nature09419)
8. Lichtenegger HC, Birkedal H, Casa DM, Cross JO, Heald SM, Waite JH, Stucky GD. 2005 Distribution of copper, zinc and iron in *Glycera* worm jaws studied with synchrotron microbeam techniques. *Chem. Mater.* **17**, 2927–2931. (doi:10.1021/cm050233v)
9. Paris O. 2008 From diffraction to imaging: new avenues to study the hierarchical structure of biological tissues with X-ray microbeams. *Biointerphases* **3**, FB1–FB26. (doi:10.1116/1.2955443)
10. Bentov S, Zaslansky P, Al-Sawalmih A, Masic A, Fratzl P, Sagi A, Berman A, Aichmayer B. 2012 Enamel-like apatite crown covering amorphous mineral in a crayfish mandible. *Nat. Commun.* **3**, 839. (doi:10.1038/ncomms1839)
11. Stock SR, De Carlo F, Almer JD. 2008 High energy X-ray scattering tomography applied to bone. *J. Struct. Biol.* **161**, 144–150. (doi:10.1016/j.jsb.2007.10.001)
12. Bleuet P, Welcomme E, Dooryhée E, Susini J, Hodeau J-L, Walter P. 2008 Probing the structure of heterogeneous diluted materials by diffraction tomography. *Nat. Mater.* **7**, 468–472. (doi:10.1038/nmat2168)
13. Stock SR, Almer JD. 2012 Diffraction microcomputed tomography of an Al-matrix SiC-monofilament composite. *J. Appl. Cryst.* **45**, 1077–1083. (doi:10.1107/S0021889812039131)
14. Álvarez-Murga M, Bleuet P, Hodeau J-L. 2012 Diffraction/scattering computed tomography for three-dimensional characterization of multi-phase crystalline and amorphous materials. *J. Appl. Cryst.* **45**, 1109–1124. (doi:10.1107/S0021889812041039)
15. Álvarez-Murga M, Bleuet P, Garbarino G, Salamat A, Mezouar M, Hodeau J-L. 2012 'Compressed graphite' formed during C_{60} to diamond transformation as revealed by scattering computed tomography. *Phys. Rev. Lett.* **109**, 025502. (doi:10.1103/PhysRevLett.109.025502)
16. Lienert U *et al*. 2011 High-energy diffraction microscopy at the advanced photon source. *JOM* **63**, 70–77. (doi:10.1007/s11837-011-0116-0)
17. Sørensen HO *et al*. 2012 Multigrain crystallography. *Z. Kristallogr.* **227**, 63–78. (doi:10.1524/zkri.2012.1438)
18. Juul Jensen D, Lauridsen EM, Margulies L, Poulsen HF, Schmidt S, Sørensen HO, Vaughan GBM. 2006 X-ray microscopy in four dimensions. *Mater. Today* **9**, 18–25. (doi:10.1016/S1369-7021(05)71334-1)
19. Mackenzie FT, Bischoff WD, Bishop FC, Loijens M, Schoonmaker J, Wollast R. 1983 Magnesian calcites: low-temperature occurrence, solubility and solid-solution behavior. In *Carbonates: mineralogy and chemistry* (ed. RJ Reeder), pp. 97–144. Washington, DC: Mineralogical Society of America.
20. Lee BP, Messersmith PB, Israelachvili JN, Waite JH. 2011 Mussel-inspired adhesives and coatings. *Annu. Rev. Mater. Res.* **41**, 99–132. (doi:10.1146/annurev-matsci-062910-100429)
21. Waite JH. 2002 Adhesion à la Moule. *Integr. Comp. Biol.* **42**, 1172–1180. (doi:10.1093/icb/42.6.1172)
22. MacDonald J, Freer A, Cusack M. 2010 Attachment of oysters to natural substrata by biologically induced marine carbonate cement. *Mar. Biol.* **157**, 2087–2095. (doi:10.1007/s00227-010-1476-7)
23. Kamino K. 2006 Barnacle underwater attachment. In *Biological adhesives* (eds AM Smith, JA Callow), pp. 145–166. Berlin, Germany: Springer.
24. Yamaguchi K. 1998 Cementation versus mobility: development of a cemented byssus and flexible mobility in *Anomia chinensis*. *Mar. Biol.* **132**, 651–661. (doi:10.1007/s002270050430)
25. Yonge CM. 1977 Form and evolution in the Anomiacea (Mollusca: Bivalvia)—*Pododesmus*, *Anomia*, *Patro*, *Enigmonia* (Anomiidae): *Placunanomia*, *Placuna* (Placunidae Fam. Nov.). *Phil. Trans. R. Soc. Lond. B* **276**, 453–523. (doi:10.1098/rstb.1977.0005)
26. Prezant RS. 1984 Functional microstructure and mineralogy of the byssal complex of *Anomia simplex* orbigny (Bivalvia: Anomiidae). *Am. Malacol. Bull.* **2**, 41–50.
27. Pujol JP, Bocquet J, Tiffon Y, Rolland M. 1970 Analyse biochimique du byssus calcifié d'*Anomia ephippium* L. (Mollusque bivalve). *Calc. Tiss. Res.* **5**, 317–326. (doi:10.1007/BF02017561)
28. Eltzholtz JR, Krogsgaard M, Birkedal H. 2009 Hierarchical design and nanomechanics of the calcified byssus of *Anomia simplex*. In *Structure–property relationships in biomineralized and biomimetic composites* (eds D Kisailus, L Estroff, W Landis, P Zavattieri, HS Gupta), pp. KK02–KK04. Warrendale, PA: Materials Research Society.
29. Eltzholtz JR, Birkedal H. 2009 Architecture of the biomineralized byssus of the saddle oyster (*Anomia* sp). *J. Adhesion* **85**, 590–600. (doi:10.1080/00218460902996820)
30. Seydel E. 1909 Untersuchungen über den Byssusapparat der Lamellibranchiaten. *Zoologische Jahrbücher* (*Jena*) **27**, 465–582. (doi:10.5962/bhl.title.11142)

31. Birkedal H, Frølich S, Leemreize H, Stallbohm R, Tseng YH. 2013 The mineralized byssus of *Anomia simplex*: a calcified attachment systems. In *Biological and biomimetic adhesives challenged and opportunities* (eds R Santos, N Aldred, S Gorb, P Flammang), pp. 16–25. London, UK: RSC publishing.
32. Pokroy B, Fitch AN, Lee PL, Quintana JP, Caspi EN, Zolotoyabko E. 2006 Anisotropic lattice distortions in mollusk-made aragonite: a widespread phenomenon. *J. Struct. Biol.* **153**, 145–150. (doi:10.1016/j.jsb.2005.10.009)
33. de Jonge MD *et al*. 2010 Quantitative 3D elemental microtomography of *Cyclotella meneghiniana* at 400-nm resolution. *Proc. Natl Acad. Sci. USA* **107**, 15 676–15 680. (doi:10.1073/pnas.1001469107)
34. Kim SA, Punshon T, Lanzirotti A, Li L, Alonso JM, Ecker JR, Kaplan J, Guerinot ML. 2006 Localization of iron in *Arabidopsis* seed requires the vacuolar membrane transporter VIT1. *Science* **314**, 1295–1298. (doi:10.1126/science.1132563)
35. Ma Y *et al*. 2009 The grinding tip of the sea urchin tooth: exquisite control over calcite crystal orientation and Mg distribution. *Proc. Natl Acad. Sci. USA* **106**, 6048–6053. (doi:10.1073/pnas.0810300106)
36. Ma Y, Cohen SR, Addadi L, Weiner S. 2008 Sea urchin tooth design: an 'all-calcite' polycrystalline reinforced fiber composite for grinding rocks. *Adv. Mater.* **20**, 1555–1559. (doi:10.1002/adma.200702842)
37. Burtorn EA, Walter LM. 1987 Relative precipitation rates of aragonite and Mg calcite from seawater: temperature or carbonate ion control? *Geology* **15**, 111–115. (doi:10.1130/0091-7613(1987)15<111:RPROAA>2.0.CO;2)